Enhancing thermoelectric performance of Sb_2Te_3 through swapped bilayer defects

Jiangjing Wang[a, b #], Chongjian Zhou[c #], Yuan Yu[b #], Yuxing Zhou[a], Lu Lu[d], Bangzhi Ge[c], Yudong Cheng[b], Chun-Lin Jia[d, e], Riccardo Mazzarello[f], Zhongqi Shi[c] *, Matthias Wuttig[b, g] *, Wei Zhang[a] *

[a] Center for Advancing Materials Performance from the Nanoscale, State Key Laboratory for Mechanical Behavior of Materials, Xi'an Jiaotong University, Xi'an 710049, China

[b] Institute of Physics IA, RWTH Aachen University, 52074 Aachen, Germany

[c] State Key Laboratory for Mechanical Behavior of Materials, Xi'an Jiaotong University, Xi'an 710049, China

[d] The School of Microelectronics, State Key Laboratory for Mechanical Behavior of Materials, Xi'an Jiaotong, University, Xi'an 710049, China

[e] Ernst Ruska-Centre for Microscopy and Spectroscopy with Electrons, Forschungszentrum Jülich GmbH, 52425 Jülich, Germany

[f] Institute for Theoretical Solid-State Physics, JARA-FIT and JARA-HPC, RWTH Aachen University, 52074 Aachen, Germany

[g] JARA-Institute: Energy-Efficient Information Technology (Green IT), Forschungszentrum Jülich GmbH, Jülich, 52428 Germany

[#]These authors contributed equally to this work.

*Corresponding author. Email: zhongqishi@mail.xjtu.edu.cn, wuttig@physik.rwth-aachen.de, wzhang0@mail.xjtu.edu.cn

Abstract:

Lattice defects are typically used to tailor the thermoelectric properties of materials. It is desirable that such defects improve the electrical conductivity, while, at the same time, reduce the thermal conductivity, for an overall improvement on the thermoelectric properties of materials. Here, we report on an extended defect in Sb_2Te_3 consisting of swapped bilayers with chemical intermixing of Sb and Te atoms, which can be generated and effectively manipulated in polycrystalline samples through synthetic methods and thermal treatments. The swapped bilayers bridge the spatial gaps between the Sb_2Te_3 quintuple-layer blocks, enhancing the charge carrier mobility and thus the electrical conductivity. These defects also result in a reduced lattice thermal conductivity through suppressing phonon transport. These synergistic effects contribute together to an improved thermoelectric quality factor and an enhanced figure of merit (zT) value in Sb_2Te_3.

Key words: thermoelectric, Sb_2Te_3, swapped bilayer, charge carrier mobility, STEM

1. Introduction

Thermoelectric materials enable a direct conversion between thermal energy and electricity, providing an effective way to recycle waste heat into electrical power or to pump heat for spot cooling on integrated circuits.[1-3] The energy conversion efficiency is evaluated by the dimensionless figure of merit, $zT=S^2\sigma T/(\kappa_{ele}+\kappa_{lat})$,[4-6] where S is the Seebeck coefficient, σ the electrical conductivity, T the absolute temperature, κ_{ele} the electronic thermal conductivity, and κ_{lat} the lattice thermal conductivity. Generally, thermoelectric properties can be predicted by the quality factor, $B \propto (m^*/m_e)^{1.5}\mu/\kappa_{lat}$, where m^* is the density-of-states effective mass, m_e is the free electron mass, and μ is the carrier mobility. Band structure and defects engineering are typically employed to optimize the quality factor either by increasing the weighted mobility ($\mu_w = (m^*/m_e)^{1.5}\mu$)[7-8] or by decreasing the lattice thermal conductivity.[9-14] Yet, these parameters are usually strongly coupled with each other.[15] Optimizing one of them may degrade the other. For instance, generating lattice defects is a typical method to scatter phonons to reduce κ_{lat}, while it also impedes the carrier mobility μ.

Layer-structured tellurides, such as Bi_2Te_3,[16-21] Sb_2Te_3,[22-23], $PbBi_{2n}Te_{1+3n}$[24] and $Ge_mSb_{2n}Te_{m+3n}$[25-27], are reported to be good thermoelectric materials. These compounds are also known as phase-change materials for nonvolatile memory applications.[28] Upon thermal annealing at 250 °C and above, a layered rhombohedral structure with various types of lattice defects form in $Ge_mSb_{2n}Te_{m+3n}$ thin films. In particular, a special type of stacking faults – swapped bilayers (SBs) across the structural gaps with strong chemical intermixing of Sb and Te atoms is consistently found, which serves as the key component for layer-switching in layered $Ge_mSb_{2n}Te_{m+3n}$.[29-33] Stacking faults could effectively alter both electrical transport and thermal vibration properties. Taking into account the fact that the

formation and annihilation of SBs can be effectively manipulated in layered $Ge_mSb_{2n}Te_{m+3n}$ thin films by the interplay between heating and electron beam irradiation effects at the nanoscale,[34-36] it is thus intriguing to assess the role of this intrinsic type of defects, which do not affect the chemical composition, in shaping the thermoelectric properties of layered telluride compounds.

In this work, we focus on Sb_2Te_3, the parent compound of $Ge_mSb_{2n}Te_{m+3n}$, as its structure and chemical composition are simpler. This compound serves as an excellent host material for phase-change memory applications[37-38] and could display good thermoelectric properties, which have been linked to the peculiar form of bonding – metavalent bonding (MVB).[39-44] In our recent work,[45] we have shown that by annealing the sputtered amorphous Sb_2Te_3 thin film (~150 nm) at 300 ºC, it is feasible to obtain SBs in large amounts. We have also elucidated that these swapping bilayers are stabilized by the chemical intermixing of Sb and Te near the structural gaps.

2. Results and discussions

Here, we carry out density-functional theory (DFT) calculations to assess the impact of SBs on the electronic structure (see Methods). We construct and optimize an ideal rhombohedral model and a defective model with six SBs, as displayed in Figure 1a and 1b. In the ideal model, three Sb_2Te_3 quintuple-layer (QL) atomic blocks and three vacant gaps are alternately stacked along the *c*-axis. The gaps are commonly known as van der Waals (vdW) gaps, but it has been shown recently that the bonding in these regions is stronger than vdW bonding[42, 46]. Therefore, we refer to them as vdW-like gaps in the following.

The charge density of the two models was calculated. Four slices across the vdW-like gaps were selected to visualize the charge distribution along the view directions, as indicated by the dashed lines in Figure 1a and 1b. The two-dimensional contour plots for these four slices are shown in

Figure 1c-f. The magnitude of charge density is depicted by a color bar ranging from 0.00 to 0.08 in the charge density contour maps. The region with larger value has more charge carriers, while those with small values represent marginal electron distribution. For the ideal model, the magnitude of charge density inside QL atomic blocks is ~0.04, and gets reduced to ~0.01 in the vdW-like gaps, as marked by the blue arrows. Regarding the defective model, the magnitude of charge density inside QL atomic blocks is also ~0.04, however, it remains large (0.02~0.04) across the gaps owing to the presence of the SBs. Such enriched charge density along the connections of atomic blocks may provide additional out-of-plane conducting channels for electron transport, thereby improving the overall electrical performance.

For practical thermoelectric applications, bulk samples are needed. As sketched in Figure 2a, high purity Sb and Te beads with the composition of 40 atomic% Sb were melted at 1000 K in an evacuated fused silica tube (~10^{-5} Torr) for 6 hours. The molten phase was then quenched down to room temperature by ice water (cooling rate of ~10^3 K/s) to generate defective Sb_2Te_3 crystals. Note that in nanoscale electronic devices, where very rapid cooling (e.g. ~10^9 K/s) could be achieved, quenching from the melt typically results in amorphous or metastable rocksalt phase of Sb_2Te_3.[38] The X-ray diffraction (XRD) measurement confirms that the quenched (q-) sample is in a single phase (Figure S1). The structural details of this q-sample were investigated at atomic level by spherical aberration corrected (Cs-corrected) scanning transmission electron microscopy (STEM) (see Methods). As shown in Figure 2b and Figure S2, the high angle annular dark field (HAADF) images taken along $[11\bar{2}0]$ direction reveal a large amount of SBs with a density ~4×10^6 m^{-1}. These SBs are sequentially and uniformly distributed along the out-of-plane direction, connecting two adjacent QL blocks, as indicated by the yellow arrows. Figure 2c presents a magnified HAADF image, showing

the atomic details of the SBs. The electron backscattered diffraction (EBSD) measurements (Figure S3) reveal that the q-sample is polycrystalline with grain size ranging mainly from ~1 to ~5 μm. The inverse pole figure of the orientation map shows that these grains are randomly oriented in the q-sample. The grain size could be adjusted by changing the rotation speed and duration of ball milling, the time window for quenching from high temperatures as well as subsequent thermal annealing. There is also increasing interest in controlling the grain size in thin film samples, which was achieved in $GeSb_2Te_4$ thin films by adjusting deposition parameters.[47]

The q-sample was annealed to tailor the density and distribution of SBs. We found that a thermal annealing at 400 ºC over 48 hours is sufficient to remove all the SBs. Figure 2d displays a typical HAADF image of the annealed (a-) sample, where SBs are not observed. Massive large-scale STEM scans confirm that SBs are rarely observed (Figure S4). The EBSD measurements demonstrate that the a-sample also has randomly orientated grains with grain size ranging mainly from ~2 to ~8 μm. The average grain size of the q- and a-samples is ~3.4 and ~5.8 μm, respectively (Figure S3). To evaluate the potential impact of grain boundaries on thermoelectric performance, we also prepared a single-crystal (s-) sample. The s-sample was prepared by re-melting (at ~1000K) and slowly unidirectionally solidifying (1mm/h) the a-sample using a Bridgeman furnace (see Methods). The single-crystal nature of the s-sample was confirmed by XRD analysis (Figure S1), and SBs were not observed in the large-scale HAADF scans (Figure S5).

Temperature-dependent Hall measurements were performed on the three samples. The Hall measurements show that all three samples are *p*-type semiconductors, which is due to the self-doping effects by Sb vacancies.[48] Figure 3a displays the carrier concentration of the three samples. The q- and a-samples show similar level of hole carriers in the measured temperature range. In comparison,

the s-sample shows higher carrier concentration, probably due to the higher amount of point defects on the Sb sublattice. However, as regards the carrier mobility, the q-sample shows higher values than the other two samples (Figure 3b), despite its smaller grain size. Clearly, grain boundary scattering cannot account for the improvement in mobility, which instead stems from intra-grain mechanisms. As predicted by DFT calculations in Figure 1e and 1f, the SBs enhance the out-of-plane transport, leading to a higher mobility of the charge carriers. Regarding the two samples that have the same perfect rhombohedral lattice, the s-sample without any grain boundary shows a slightly higher mobility value, as expected. Overall, the q-sample shows higher electrical conductivity σ values than the a-sample but smaller values with respect to the s-sample at all measured temperatures, due to the lower carrier concentration (Figure 3c).

Figure 3d presents the profiles of the Seebeck coefficient S. All the three samples show positive values, due to the *p*-type transport behavior. The Seebeck coefficient presents an inverse trend relative to the electrical conductivity, as normally observed in semiconductors. As shown in Figure 3e, we also analyzed the density-of-states effective mass by calculating the Pisarenko plot based on the single parabolic band (SPB) model with acoustic phonon-dominated carrier scattering,[49] which has been verified by the exponentially decreasing electrical conductivity with a temperature dependence of $T^{-1.5}$ in Figure 3c. The result shows that the q-sample tends to have a lower effective mass than the other two samples, while the a- and s-samples show a very similar value. The low effective mass of the q-sample is consistent with its measured high carrier mobility. As a result of the tradeoff between σ and S, all the three samples show comparable power factor in the measured temperature range (Figure 3f).

We also carried out temperature-dependent thermal conductivity measurements for the three samples

(Figure 4a). As expected, the s-sample shows much higher values of thermal conductivity κ_{tot} ($\kappa_{ele}+\kappa_{lat}$) than the other two samples due to its minor amount of defects. The q-sample shows slightly smaller κ_{tot} values, but much smaller lattice thermal conductivity κ_{lat} values, with respect to the a-sample. κ_{ele} is proportional to σ according to the Wiedemann-Franz law, implying that a larger σ corresponds to a higher κ_{ele}. The q-sample presents a much larger σ but slightly lower κ_{tot} as compared with the a-sample, indicating that phonon transport is significantly suppressed in the q-sample. From the Wiedemann-Franz law, we can separate the phonon contribution to the thermal transport by subtracting κ_{ele} from κ_{tot} (see Methods). Figure 4b and Figure S6 present the κ_{lat} and κ_{ele} profiles, respectively. The q-sample exhibits the expected higher κ_{ele} (1.93 W m^{-1} K^{-1}) compared with the a-sample (1.42 W m^{-1} K^{-1}) at room temperature due to the higher σ. The annealed sample shows a κ_{lat} value of 2.05 W m^{-1} K^{-1} at room temperature, while the quenched sample shows a value of 1.36 W m^{-1} K^{-1} only, corresponding to a difference of ~35%. This demonstrates that the SBs can effectively suppress the lattice thermal conductivity in Sb_2Te_3.

To gain further understanding of the bilayer effects on κ_{lat}, we use the Debye-Callaway model to fit the experimental data[50],

$$\kappa_{lat} = \frac{k_B}{2\pi^2 \upsilon}\left(\frac{k_B T}{\hbar}\right)^3 \int_0^{\theta_D/T} \tau_{tot}(x)\frac{x^4 e^x}{(e^x-1)^2}dx \qquad \text{Equation 1}$$

where k_B is the Boltzmann constant, υ the average sound velocity, $\hbar$ the reduced Plank's constant, θ_D the Debye temperature, $x = \hbar\omega/k_BT$, ω the angular frequency of phonons, and τ_{tot} the total relaxation time.[49] The phonon scattering sources include the Normal (N) and Umklapp (U) processes, grain boundaries (GB) and swapped bilayer stacking faults (SF), according to the Matthiessen's rule $\tau_{tot}^{-1} = \tau_N^{-1} + \tau_U^{-1} + \tau_{GB}^{-1} + \tau_{SF}^{-1}$ (see Methods). The s-sample only involves the N and U terms, and the GB term is considered for the a-samples. For the q-sample, we also include the SF term with density of 4×10^6

m^{-1}. The purple, green and red dashed lines in Figure 4b represent the calculated results for the s-, a- and q-samples, respectively. The calculations fit very well to the experimental data, indicating that the observed SBs are indeed responsible for the reduced lattice thermal conductivity κ_{lat}. The contribution of specific defects can be further revealed by the spectral lattice thermal conductivity (κ_s). Figure 4c shows the calculated κ_s at 300 K for the q-sample (see Methods). The pink and light green areas correspond to the reduced κ_{lat} induced by GB and SF, respectively. These calculations indicate that grain boundaries have marginal effects on the phonon transport. In contrast, the SBs strongly suppress the heat-carrying phonons over the entire phonon spectrum for reduced κ_{lat}.

The maximum thermoelectric performance can be quantified by the quality factor B described by the following expression[51-52]

$$B = 5.745 \times 10^{-6} \cdot \frac{\mu (m^*/m_e)^{1.5} T^{2.5}}{\kappa_{lat}} = 5.745 \times 10^{-6} \cdot T^{2.5} \cdot \frac{\mu_w}{\kappa_{lat}} \qquad \text{Equation 2}$$

Figure 4d shows the weighted mobility μ_w and quality factor B calculated for the three samples at room temperature. The three samples show nearly identical μ_w, indicating similar power factor. However, the q-sample exhibits a much higher quality factor than the s- and a-samples, which is mainly contributed by the increased charge carrier mobility and decreased lattice thermal conductivity induced by the SBs. We also used a more general model proposed in Ref.[53], and the calculated μ_w and B are consistent (Figure S7). As a result, the final zT value in the q-sample is the highest, especially at high temperatures, see Figure 4e. The swapped-bilayers thus optimize both the carrier mobility and the lattice thermal conductivity. Further alloying and doping are expected to lead to further improvement on the zT values.[54-55]

3. Conclusion

In conclusion, we have proposed a strategy of heat treatment to control the formation and annihilation of SBs in bulk Sb_2Te_3, which was evidenced by the atomic-level resolution STEM-HAADF characterization. We also demonstrated that the SBs connect the weakly coupled van der Waals-like gaps and thus provide additional conducting channels for electron transport along the out-of-plane direction due to the strong Sb-Te chemical intermixing. Thermoelectric performance measurements reveal that the bilayers could effectively enhance the carrier transport to improve the electrical conductivity, while impeding the phonon transport over the entire phonon spectrum and thus lowering the lattice thermal conductivity. As a result, the quality factor is greatly improved and an enhanced thermoelectric performance is achieved. We also note that such bilayers are frequently observed in IV-V-chalcogenides and binary V-chalcogenides based phase change materials, such as Sb_2Te_3,[45] Bi_2Te_3,[56] $GeSb_2Te_4$,[29-30] and $Ge_2Sb_2Te_5$[34-35]. Our work provides an effective experimental procedure to engineer these extended defects in layered chalcogenide materials, which could potentially be coupled with other point defects engineering approaches[57-59], to achieve improved thermoelectric performances for practical applications, such as wearable electrocardiographic applications[60].

4. Experimental section

Sample synthesis：

The Sb_2Te_3 ingots were synthesized by melting the precursor beads with appropriate molar ratio of constituent elements of Sb, and Te (99.999%, American Elements) in an evacuated fused silica tube (~10^{-5} Torr) at 1000K for 6h. The melts were quenched in ice water (denoted as quenched sample, q-sample). The q-samples were subsequently annealed at 673K for 48h and then naturally cooled to ambient temperature (marked as annealed sample, a-sample). The obtained ingots were manually

ground using an agate mortar and pestle to obtain fine powder in an Ar-filled glove box. The resulting powder was loaded in a graphite module and densified at 723K for 5 min under an axial pressure of 50 MPa in a vacuum using spark plasma sintering (SPS) (SPS-211Lx, Fuji Electronic Industrial Co., Japan). Afterwards, a cylindrical sample with a thickness of ~12.7 mm and a diameter of 12 mm was obtained. The single crystal sample (s-sample) was prepared from the a-sample, which was sealed in an evacuated cone-shaped tube and put into a Bridge man furnace. The tube vertically passes through the flat-temperature zone of 1000K in a velocity of 1mm/h, leading to a unidirectional solidification of the melts to form large single crystal. The density of the samples was calculated from the geometrical volume and masses, and all the samples have density higher than 99.5% of the theoretical value.

Experimental methods:

Transmission electron microscopy (TEM): The TEM specimens were prepared by a dual beam focused ion beam (FIB) system (Helios NanoLab 600i, FEI) with a Ga ion beam at 30 kV beam energy, the specimens were further polishing under 5 and 2 kV to clean the surface and remove the gallium ion damage[61]. Atomic-resolution STEM-HAADF imaging experiments were performed on a JEOL ARM200F STEM with a probe aberration corrector, operated at 200 keV.

Electron back-scatter diffraction (EBSD): The samples for EBSD measurements were mechanically polished by SiC paper and diamond paste (1 μm in roughness) and fine polished using silica and 30% H_2O_2. The EBSD measurements were carried out on a dual beam focused ion beam (FIB) system (Helios NanoLab 600i, FEI) using a Hikari S/N 1040 camera (TSL/EDAX) with OIM Data Collection software for the data acquisition and OIM Analysis 7 software for the data analysis.

X-ray Diffraction (XRD): XRD patterns for q- and a-samples were collected on a SmartLab Rigaku

powder X-ray diffractometer equipped with a Cu Kα (l = 1.5418 Å) graphite monochromator operating at 40 kV and 20 mA. For the s-sample, the XRD pattern was recorded on a cleaved piece along the (0003) direction. The XRD measurements confirm the single-phase nature of the three samples.

Thermoelectric property measurements: The thermal conductivity for polycrystalline samples were measured along the direction perpendicular the pressure direction, and thermal conductivity for s-sample was determined along the cleavage plane (in-plane). The thermal diffusivities were measured using laser flash method in a Netsch LFA 457 equipment, and the samples are in form of disk form with a diameter of 8 mm and a thickness of ~2 mm. The thermal conductivity was calculated by $\kappa = D\rho C_p$, where D is the diffusivity, ρ is the sample density measured by mass and volume, and C_p is the heat capacity obtained using Dulong-Petit limit.

The measurements of electrical conductivities were carried out in a ZEM-3 apparatus using standard four-probe methods in an inert Helium atmosphere. The samples were cut and polished into rectangular columns with a size about 12 × 2 × 2 mm^3. Electrical contacts were made using Pt/Rh and Pt that were mechanically contacted to the rectangular columns without application of a paste that typically contains organic solvents.

Hall effect were measured as a function of temperature using van der Pauw method on a Lakeshore 8407 system from 300 to 773 K under an ultrahigh vacuum (<10^{-5} Pa) with a reversible 1.5 T magnetic field and 15 mA excitation current. The samples were in form of a disk with diameter of 8 mm and a thickness below 1mm.

Theoretical calculations of thermal conductivities: We used Debye-Callaway model to fit the experimental data. According to the Matthiessen's rule, to calculate the total relaxation time τ_{tot}, we

firstly calculated the relaxation time associated with Umklapp (τ_U) and Normal (τ_N) phonon-phonon scattering from

$$\tau_U^{-1} + \tau_N^{-1} = A_N \frac{2}{(6\pi^2)^{1/3}} \frac{k_B \bar{V}^{1/3} \gamma^2 \omega^2 T}{\bar{M} v^3} \qquad \text{Equation 2}$$

where A_N is an additional factor (=1.1 in this case fitted with the single crystal data) for integrating (τ_U) and (τ_N), $\bar{V}$ is the average atomic volume of Sb_2Te_3, γ is the Grüneisen parameter (2.3), $\bar{M}$ is the average atomic mass.

The relaxation time associated with grain boundary scattering is given by

$$\tau_{GB}^{-1} = v/d \qquad \text{Equation 3}$$

where *d* is the average grain size. The *d* values of q- and a- samples are measured as 3.4 μm and 5.8 μm through EBSD analyses, respectively (Figure S3b and d).

Compared with the s-sample, the slightly decreased lattice thermal conductivity in the a-sample is mainly due to the increased density of grain boundaries. For q-sample, the total phonon relaxation time of swapped bilayers stacking fault (SF) phonon scattering was considered. The SF scattering rate for phonons is:

$$\tau_{SF}^{-1} = 0.7 \frac{a^2 \gamma^2 N_{SF}}{v} \omega^2 \qquad \text{Equation 4}$$

where *a* is the lattice parameter, N_{SF} is the density of bilayer stacking fault, which is determined to be 4×10^6 m^{-1}.

DFT calculations:

The models of Sb_2Te_3 rhombohedral ideal structure and defective structure with swapped bilayers (SBs) were built in an orthorhombic unit-cell with experimentally determined lattice parameter (a=12.78 Å, b=25.51 Å, c=30.45 Å), containing 15 atomic layers with 144 Sb and 216 Te atoms. Three Sb_2Te_3 quintuple-layer (QL) atomic blocks and three vacant gaps are alternatively stacked

along c axis. In the model of defective structure, we constructed the SBs by swapping parts of outmost Te and sub-outer Sb layers of QL blocks, which connects two adjacent QL atomic blocks horizontally. Each bilayer was constructed with 2 Sb-Te units and the Sb-Te intermixing is made in the bilayer regions. DFT calculations were performed utilizing the Perdew-Burke-Ernzerhof functionals and the projected augmented plane-wave (PAW) pseudopotentials, which is implemented in the Vienna ab initio simulation package (VASP). The cut-off energy for the plane-wave basis expansion was set to be 500 eV. The Brillouin zoom was only sampled at Γ point. Self-consistent calculations and relaxation calculations were carried out with a Gaussian smearing width of 0.1 eV and a convergence tolerance of 1×10^{-7} eV. The van der Waals correction was implemented using DFT-D3 method.

Acknowledgements

The authors thank Shixuan Liu from Shaanxi Normal University for the support during thermoelectric performance measurements. W.Z. acknowledges the support of National Natural Science Foundation of China (61774123), 111 Project 2.0 (BP2018008). Z.S. acknowledges the support of National Natural Science Foundation of China (51872222) and the Shaanxi Innovation Capacity Support Program (2018TD-031). C.-L.J., R.M., and M.W. acknowledge funding from Deutsche Forschungsgemeinschaft within SFB 917 “Nanoswitches”. The authors also acknowledge the support by the Materials Studio for Neuro-inspired Computing (mSonic), the International Joint Laboratory for Micro/Nano Manufacturing and Measurement Technologies of Xi’an Jiaotong University. The authors also acknowledge the computational resources provided by the HPC platform of Xi’an Jiaotong University.

References

1. Y. Xiao, L. D. Zhao, Seeking New, Highly Effective Thermoelectrics. Science 367 (2020) 1196-1197.
2. X. L. Shi, J. Zou, Z. G. Chen, Advanced Thermoelectric Design: From Materials and Structures to Devices. Chem. Rev. (2020) DOI: 10.1021/acs.chemrev.0c00026.
3. C. Chang, M. Wu, D. He, Y. Pei, C.-F. Wu, X. Wu, H. Yu, F. Zhu, K. Wang, Y. Chen, L. Huang, J.-F. Li, J. He, L.-D. Zhao, 3D charge and 2D phonon transports leading to high out-of-plane ZT in n-type SnSe crystals. Science 360 (2018) 778.
4. W. D. Liu, D. Z. Wang, Q. Liu, W. Zhou, Z. Shao, Z. G. Chen, High-Performance GeTe-Based Thermoelectrics: from Materials to Devices. Adv. Energy Mater. 10 (2020) 2000367.
5. Y. Wang, L. Yang, X. L. Shi, X. Shi, L. Chen, M. S. Dargusch, J. Zou, Z. G. Chen, Flexible Thermoelectric Materials and Generators: Challenges and Innovations. Adv. Mater. 31 (2019) 1807916.
6. G. Tan, L. D. Zhao, M. G. Kanatzidis, Rationally Designing High-Performance Bulk Thermoelectric Materials. Chem. Rev. 116 (2016) 12123-12149.
7. C. Zhou, Y. K. Lee, J. Cha, B. Yoo, S. P. Cho, T. Hyeon, I. Chung, Defect Engineering for High-Performance n-Type PbSe Thermoelectrics. J. Am. Chem. Soc. 140 (2018) 9282-9290.
8. Y. Qin, Y. Xiao, L.-D. Zhao, Carrier mobility does matter for enhancing thermoelectric performance. APL Mater. 8 (2020) 010901.
9. J. Zhang, D. Wu, D. He, D. Feng, M. Yin, X. Qin, J. He, Extraordinary Thermoelectric Performance Realized in n-Type PbTe through Multiphase Nanostructure Engineering. Adv. Mater. 29 (2017) 1703148.
10. J. Li, Z. Chen, X. Zhang, H. Yu, Z. Wu, H. Xie, Y. Chen, Y. Pei, Simultaneous Optimization of Carrier Concentration and Alloy Scattering for Ultrahigh Performance GeTe Thermoelectrics. Adv. Sci. 4 (2017) 1700341.
11. M. Hong, Y. Wang, S. Xu, X. Shi, L. Chen, J. Zou, Z.-G. Chen, Nanoscale pores plus precipitates rendering high-performance thermoelectric SnTe1-xSex with refined band structures. Nano Energy 60 (2019) 1-7.
12. M. Ibanez, R. Hasler, A. Genc, Y. Liu, B. Kuster, M. Schuster, O. Dobrozhan, D. Cadavid, J. Arbiol, A. Cabot, M. V. Kovalenko, Ligand-Mediated Band Engineering in Bottom-Up Assembled SnTe Nanocomposites for Thermoelectric Energy Conversion. J. Am. Chem. Soc. 141 (2019) 8025-8029.
13. W. He, D. Wang, H. Wu, Y. Xiao, Y. Zhang, D. He, Y. Feng, Y.-J. Hao, J.-F. Dong, R. Chetty, L. Hao, D. Chen, J. Qin, Q. Yang, X. Li, J.-M. Song, Y. Zhu, W. Xu, C. Niu, X. Li, G. Wang, C. Liu, M. Ohta, S. J. Pennycook, J. He, J.-F. Li, L.-D. Zhao, High thermoelectric performance in low-cost SnS0.91Se0.09 crystals. Science 365 (2019) 1418-1424.
14. J. Yang, X. Zhang, G. Liu, L. Zhao, J. Liu, Z. Shi, J. Ding, G. Qiao, Multiscale structure and band configuration tuning to achieve high thermoelectric properties in n-type PbS bulks. Nano Energy 74 (2020) 104826.
15. T. Zhu, Y. Liu, C. Fu, J. P. Heremans, G. J. Snyder, X. Zhao, Compromise and Synergy in High-Efficiency Thermoelectric Materials. Adv. Mater. 29 (2017) 1605884.
16. D. WRIGHT, Thermoelectric Properties of Bismuth Telluride and its Alloys. Nature 181 (1958) 834.
17. I. T. Witting, F. Ricci, T. C. Chasapis, G. Hautier, G. J. Snyder, The Thermoelectric Properties of n-Type Bismuth Telluride: Bismuth Selenide Alloys Bi2Te3-x Sex. Research 2020 (2020) 4361703.
18. B. Zhu, Z.-Y. Huang, X.-Y. Wang, Y. Yu, L. Yang, N. Gao, Z.-G. Chen, F.-Q. Zu, Attaining ultrahigh thermoelectric performance of direction-solidified bulk n -type Bi 2 Te 2.4 Se 0.6 via its liquid state treatment. Nano Energy 42 (2017) 8-16.
19. B. Zhu, X. Liu, Q. Wang, Y. Qiu, Z. Shu, Z. Guo, Y. Tong, J. Cui, M. Gu, J. He, Realizing record high performance in n-type Bi2Te3-based thermoelectric materials. Energy Environ. Sci. (2020) DOI: 10.1039/D0EE01349H.
20. H.-L. Zhuang, Y. Pan, F.-H. Sun, J. Dong, J. Pei, Asfandiyar, B. Cai, H. Hu, H. Tang, J.-F. Li, Thermoelectric Cu-doped (Bi,Sb)2Te3: Performance enhancement and stability against high electric current pulse. Nano Energy 60 (2019) 857-865.
21. B. Jabar, X. Qin, D. Li, J. Zhang, A. Mansoor, H. Xin, C. Song, L. Huang, Achieving high thermoelectric

performance through constructing coherent interfaces and building interface potential barriers in n-type Bi2Te3/Bi2Te2.7Se0.3 nanocomposites. J. Mater. Chem. A 7 (2019) 19120-19129.
22. Z. Li, N. Miao, J. Zhou, Z. Sun, Z. Liu, H. Xu, High thermoelectric performance of few-quintuple Sb2Te3 nanofilms. Nano Energy 43 (2018) 285-290.
23. X. Y. Wang, H. J. Wang, B. Xiang, L. W. Fu, H. Zhu, D. Chai, B. Zhu, Y. Yu, N. Gao, Z. Y. Huang, F. Q. Zu, Thermoelectric Performance of Sb2Te3-Based Alloys is Improved by Introducing PN Junctions. ACS Appl. Mater. Interfaces 10 (2018) 23277-23284.
24. B. Xu, M. T. Agne, T. Feng, T. C. Chasapis, X. Ruan, Y. Zhou, H. Zheng, J.-H. Bahk, M. G. Kanatzidis, G. J. Snyder, Y. Wu, Nanocomposites from Solution-Synthesized PbTe-BiSbTe Nanoheterostructure with Unity Figure of Merit at Low-Medium Temperatures (500–600 K). Adv. Mater. (2017) 1605140.
25. K. S. Siegert, F. R. Lange, E. R. Sittner, H. Volker, C. Schlockermann, T. Siegrist, M. Wuttig, Impact of vacancy ordering on thermal transport in crystalline phase-change materials. Rep. Prog. Phys. 78 (2014) 013001.
26. D. Wu, L. Xie, X. Xu, J. He, High Thermoelectric Performance Achieved in GeTe-Bi2Te3 Pseudo-Binary via Van der Waals Gap-Induced Hierarchical Ferroelectric Domain Structure. Adv. Funct. Mater. 29 (2019) 1806613.
27. D. Wu, L. D. Zhao, S. Hao, Q. Jiang, F. Zheng, J. W. Doak, H. Wu, H. Chi, Y. Gelbstein, C. Uher, C. Wolverton, M. Kanatzidis, J. He, Origin of the High Performance in GeTe-Based Thermoelectric Materials upon Bi2Te3 Doping. J. Am. Chem. Soc. 136 (2014) 11412-11419.
28. W. Zhang, R. Mazzarello, M. Wuttig, E. Ma, Designing crystallization in phase-change materials for universal memory and neuro-inspired computing. Nat. Rev. Mater. 4 (2019) 150–168.
29. J. Momand, R. Wang, J. E. Boschker, M. A. Verheijen, R. Calarco, B. J. Kooi, Dynamic reconfiguration of van der Waals gaps within GeTe-Sb2Te3 based superlattices. Nanoscale 9 (2017) 8774-8780.
30. J.-J. Wang, J. Wang, H. Du, L. Lu, P. C. Schmitz, J. Reindl, A. M. Mio, C.-L. Jia, E. Ma, R. Mazzarello, M. Wuttig, W. Zhang, Genesis and Effects of Swapping Bilayers in Hexagonal GeSb2Te4. Chem. Mater. 30 (2018) 4770-4777.
31. A. Lotnyk, T. Dankwort, I. Hilmi, L. Kienle, B. Rauschenbach, Atomic-scale observation of defects motion in van der Waals layered chalcogenide based materials. Scr. Mater. 166 (2019) 154-158.
32. X. Chen, J. Shen, S. Jia, Y. Zheng, S. Lv, Z. Song, M. Zhu, Observation of van der Waals reconfiguration in superlattice phase change materials. Nanoscale 11 (2019) 16954-16961.
33. X.-B. Li, N.-K. Chen, X.-P. Wang, H.-B. Sun, Phase-Change Superlattice Materials toward Low Power Consumption and High Density Data Storage: Microscopic Picture, Working Principles, and Optimization. Adv. Funct. Mater. 28 (2018) 1803380.
34. A. Lotnyk, U. Ross, T. Dankwort, I. Hilmi, L. Kienle, B. Rauschenbach, Atomic structure and dynamic reconfiguration of layered defects in van der Waals layered Ge-Sb-Te based materials. Acta Mater. 141 (2017) 92-96.
35. A. Lotnyk, T. Dankwort, I. Hilmi, L. Kienle, B. Rauschenbach, In situ observations of the reversible vacancy ordering process in van der Waals-bonded Ge–Sb–Te thin films and GeTe–Sb2Te3 superlattices. Nanoscale 11 (2019) 10838-10845.
36. A. Lotnyk, M. Behrens, B. Rauschenbach, Phase change thin films for non-volatile memory applications. Nanoscale Adv. 1 (2019) 3836-3857.
37. K. Ding, J. Wang, Y. Zhou, H. Tian, L. Lu, R. Mazzarello, C. Jia, W. Zhang, F. Rao, E. Ma, Phase-change heterostructure enables ultralow noise and drift for memory operation. Science 366 (2019) 210-215.
38. F. Rao, K. Ding, Y. Zhou, Y. Zheng, M. Xia, S. Lv, Z. Song, S. Feng, I. Ronneberger, R. Mazzarello, W. Zhang, E. Ma, Reducing the stochasticity of crystal nucleation to enable subnanosecond memory writing. Science 358 (2017) 1423-1427.
39. J. Y. Raty, M. Schumacher, P. Golub, V. L. Deringer, C. Gatti, M. Wuttig, A Quantum-Mechanical Map for Bonding and Properties in Solids. Adv. Mater. 31 (2019) 1806280.

40. M. Wuttig, V. L. Deringer, X. Gonze, C. Bichara, J. Y. Raty, Incipient Metals: Functional Materials with a Unique Bonding Mechanism. Adv. Mater. 30 (2018) 1803777.
41. M. Cagnoni, D. Fuhren, M. Wuttig, Thermoelectric Performance of IV-VI Compounds with Octahedral-Like Coordination: A Chemical-Bonding Perspective. Adv. Mater. 30 (2018) 1801787.
42. Y. Cheng, O. Cojocaru-Miredin, J. Keutgen, Y. Yu, M. Kupers, M. Schumacher, P. Golub, J. Y. Raty, R. Dronskowski, M. Wuttig, Understanding the Structure and Properties of Sesqui-Chalcogenides (i.e., V2VI3 or Pn2Ch3 (Pn=Pnictogen, Ch=Chalcogen) Compounds) from a Bonding Perspective. Adv. Mater. 31 (2019) 1904316.
43. Y. Yu, M. Cagnoni, O. Cojocaru-Mirédin, M. Wuttig, Chalcogenide Thermoelectrics Empowered by an Unconventional Bonding Mechanism. Adv. Funct. Mater. 30 (2020) 1904862.
44. B. J. Kooi, M. Wuttig, Chalcogenides by Design: Functionality through Metavalent Bonding and Confinement. Adv. Mater. 32 (2020) 1908302.
45. J.-J. Wang, J. Wang, Y. Xu, T. Xin, Z. Song, M. Pohlmann, M. Kaminski, L. Lu, H. Du, C.-L. Jia, R. Mazzarello, M. Wuttig, W. Zhang, Layer-Switching Mechanisms in Sb2Te3. Phys. Status Solidi RRL 13 (2019) 1900320.
46. A. M. Mio, P. M. Konze, A. Meledin, M. Küpers, M. Pohlmann, M. Kaminski, R. Dronskowski, J. Mayer, M. Wuttig, Impact of Bonding on the Stacking Defects in Layered Chalcogenides. Adv. Funct. Mater. 29 (2019) 1902332.
47. M. M. Dück, T. Schäfer, S. Jakobs, C. F. Schön, H. Niehaus, O. Cojocaru-Mirédin, M. Wuttig, Disorder Control in Crystalline GeSb2Te4 and its Impact on Characteristic Length Scales. physica status solidi (RRL) – Rapid Research Letters 13 (2019).
48. Y. Jiang, Y. Y. Sun, M. Chen, Y. Wang, Z. Li, C. Song, K. He, L. Wang, X. Chen, Q. K. Xue, X. Ma, S. B. Zhang, Fermi-level tuning of epitaxial Sb2Te3 thin films on graphene by regulating intrinsic defects and substrate transfer doping. Phys. Rev. Lett. 108 (2012) 066809.
49. Y. Yu, D.-S. He, S. Zhang, O. Cojocaru-Mirédin, T. Schwarz, A. Stoffers, X.-Y. Wang, S. Zheng, B. Zhu, C. Scheu, D. Wu, J.-Q. He, M. Wuttig, Z.-Y. Huang, F.-Q. Zu, Simultaneous optimization of electrical and thermal transport properties of Bi 0.5 Sb 1.5 Te 3 thermoelectric alloy by twin boundary engineering. Nano Energy 37 (2017) 203-213.
50. J. Callaway, H. C. von Baeyer, Effect of point imperfections on lattice thermal conductivity. Phys. Rev. 120 (1960) 1149.
51. R. P. Chasmar, R. Stratton, The Thermoelectric Figure of Merit and its Relation to Thermoelectric Generators. J. Electron. Control 7 (1959) 52-72.
52. M. Hong, Z.-G. Chen, S. Matsumura, J. Zou, Nano-scale dislocations induced by self-vacancy engineering yielding extraordinary n -type thermoelectric Pb 0.96-y In y Se. Nano Energy 50 (2018) 785-793.
53. S. Dongmin Kang, G. Jeffrey Snyder, Charge-transport model for conducting polymers. Nat Mater 16 (2017) 252-257.
54. C. Li, S. Ma, P. Wei, W. Zhu, X. Nie, X. Sang, Z. Sun, Q. Zhang, W. Zhao, Magnetism-induced huge enhancement of the room-temperature thermoelectric and cooling performance of p-type BiSbTe alloys. Energy Environ. Sci. 13 (2020) 535-544.
55. H. Wu, X. Lu, G. Wang, K. Peng, B. Zhang, Y. Chen, X. Gong, X. Tang, X. Zhang, Z. Feng, G. Han, Y. Zhang, X. Zhou, Strong lattice anharmonicity securing intrinsically low lattice thermal conductivity and high performance thermoelectric SnSb2Te4 via Se alloying. Nano Energy 76 (2020) 105084.
56. Y. Jiang, Y. Wang, J. Sagendorf, D. West, X. Kou, X. Wei, L. He, K. L. Wang, S. Zhang, Z. Zhang, Direct atom-by-atom chemical identification of nanostructures and defects of topological insulators. Nano Lett. 13 (2013) 2851–2856.
57. Y. Wang, W.-D. Liu, X.-L. Shi, M. Hong, L.-J. Wang, M. Li, H. Wang, J. Zou, Z.-G. Chen, Enhanced thermoelectric properties of nanostructured n-type Bi2Te3 by suppressing Te vacancy through non-equilibrium fast reaction. Chemical Engineering Journal 391 (2020).

58. Y. Wang, M. Hong, W.-D. Liu, X.-L. Shi, S.-D. Xu, Q. Sun, H. Gao, S. Lu, J. Zou, Z.-G. Chen, Bi0.5Sb1.5Te3/PEDOT:PSS-based flexible thermoelectric film and device. Chemical Engineering Journal 397 (2020).
59. M. Hong, W. Lyv, M. Li, S. Xu, Q. Sun, J. Zou, Z.-G. Chen, Rashba Effect Maximizes Thermoelectric Performance of GeTe Derivatives. Joule 4 (2020) 2030-2043.
60. M. Dargusch, W. D. Liu, Z. G. Chen, Thermoelectric Generators: Alternative Power Supply for Wearable Electrocardiographic Systems. Advanced Science 7 (2020).
61. J. Mayer, L. A. Giannuzzi, T. Kamino, J. Michael, TEM Sample Preparation and FIB-Induced Damage. MRS Bulletin 32 (2007) 400-407.

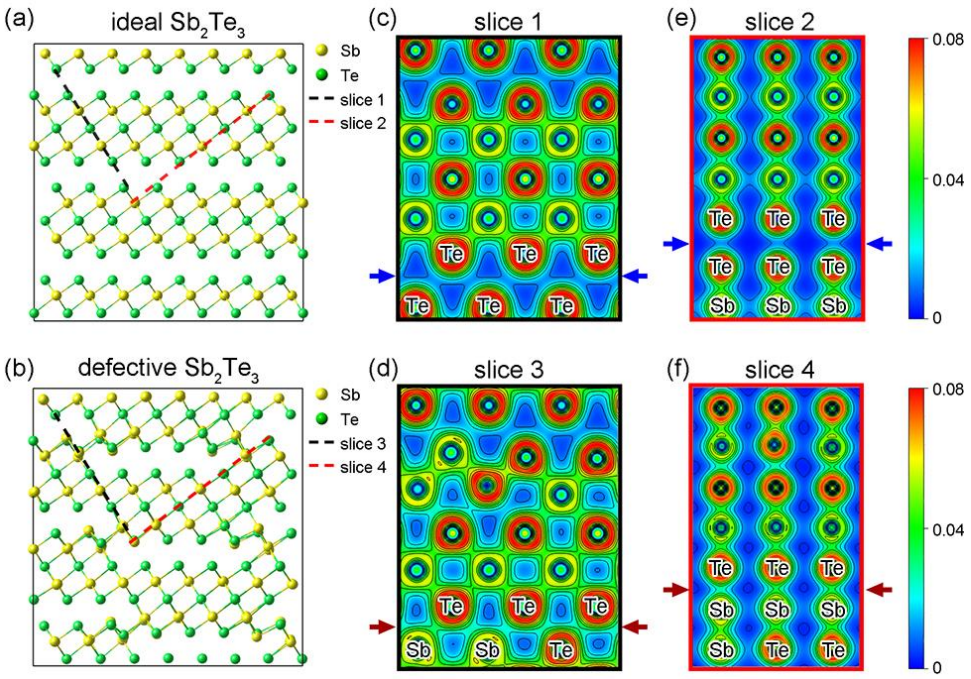

Figure 1. Atomic models and charge density maps. (a) The ideal atomic model of Sb_2Te_3. (b)The defective model with three pairs of swapped bilayer defects. (c)-(f) The two-dimensional charge density contour maps for slices 1-4 in (a) and (b), respectively. The blue and red arrows mark similar regions in two models, corresponding to vdW-like gaps in the ideal model and the SBs in the defective model, respectively. Due to the Sb-Te intermixing, the charge density between the adjacent blocks increases in bilayer regions, indicating that the electron transport is enhanced by the bilayers along the out-of-plane direction.

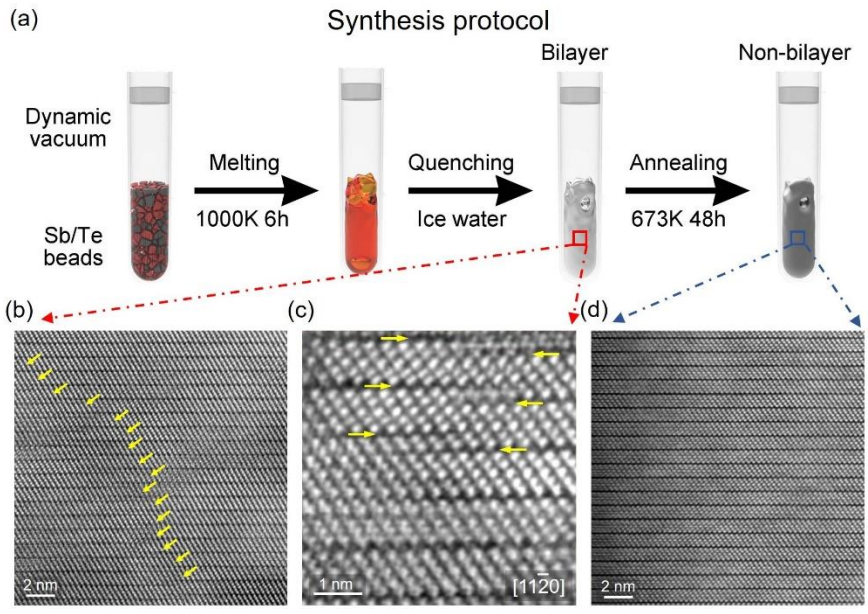

Figure 2. Synthesis protocol and atomic-resolution imaging of Sb_2Te_3 samples. (a) Schematic diagram of the sample synthesis protocol for quenched and annealed samples. (b) The large scale STEM-HAADF image of the q-sample recorded along the [11$\bar{2}$0] direction. A series of continuous bilayers can be observed, as marked by yellow arrows. (c) The atomic-resolution HAADF image of the bilayers in the q-sample. The vdW-like gaps are indicated by yellow arrows. (d) The large scale HAADF image of the annealed polycrystalline sample: no obvious bilayers can be observed in the sample.

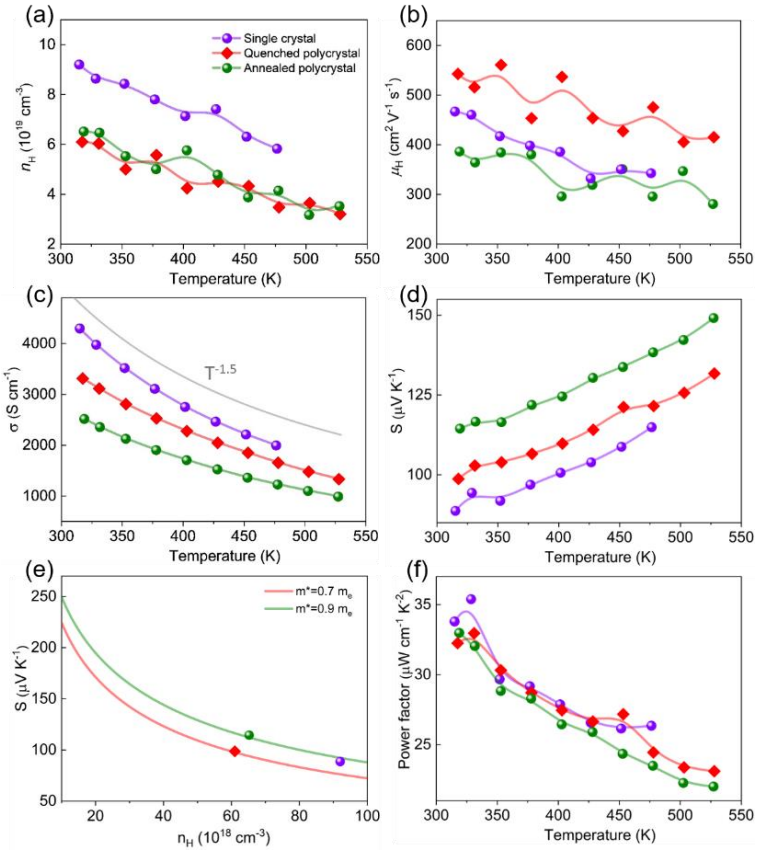

Figure 3. Hall effect measurements and temperature-dependent electrical transport properties for the three samples. (a) Hall carrier concentration as a function of temperature; (b) Hall carrier mobility; (c) Temperature-dependent electrical conductivity; (d) Seebeck coefficient; (e) Pisarenko plot calculated based on the SPB model; (f) Temperature-dependent power factor. The electrical conductivity of the single crystal sample follows the trend of $T^{-1.5}$, indicating that the acoustic phonons dominated the charge carrier scattering.

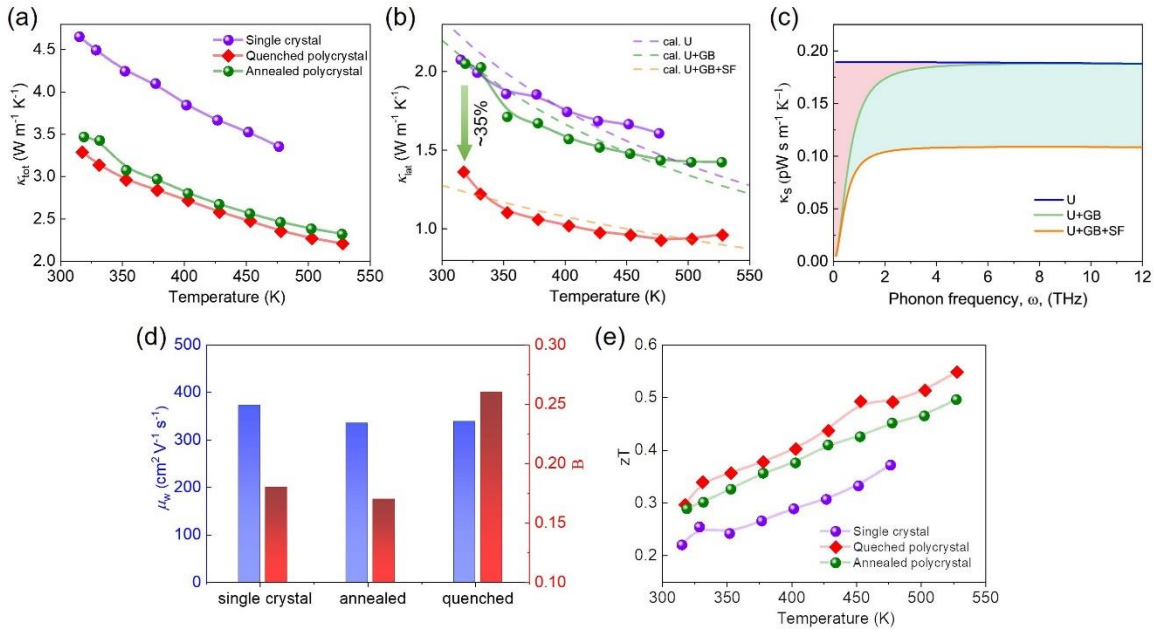

Figure 4. Thermal conductivity as a function of temperature and thermoelectric performances. (a) Total thermal conductivity. (b) Lattice thermal conductivity. The dashed lines depict the results calculated by the

Debye-Callaway's model. (c) Spectral lattice thermal conductivity at room temperature showing the individual contributions of grain boundaries (GB) and swapped bilayer stacking faults (SF) to the reduced lattice thermal conductivity. The pink region indicates the thermal conductivity reduced by GB, and the cyan region indicates that reduced by SF. (d) Weighted mobility and quality factor at room temperature. The quality factor of the q-sample shows a significant improvement, although the weighted mobility is similar to the other two samples. (e) zT values as a function of temperature.